Supporting Information

Topological Carbon Nitride: Localized Photon Absorption and Delocalized Charge Carrier Separation at Intertwined Photocatalyst Interface

M. Z. Rahman[a,b*], J. Moffatt[c] and N. Spooner[c]

E-mail: mohammad.rahman@adelaide.edu.au

[a]John J. Mcketta Department of Chemical Engineering and Department of Chemistry, University of Texas at Austin, TX 78712-1589, USA

[b]School of Chemical Engineering, The University of Adelaide, SA 5005, Australia

[c]Institute for Photonics and Advanced Sensing, The University of Adelaide, SA 5005, Australia

This supporting information contains following contents:

I. Experimental Section

a. Synthesis of TCN

The synthesis of TCN was accomplished following two consecutive steps. First we have synthesized GCN via polycondensation and polymerization of dicyandiamide (DCDA). For this purpose, 15 g of DCDA was heated in a tube furnace under N_2 flow at 550 ^oC with a heat ramp rate of 2.3 ^oC/min for 4.5 h. When the furnace cooled down to room temperature (RT), then GCN was collected. In the final step, 4 g of as-prepared GCN was mixed with 2 g of melamine in 25 mL of deionized water (DI) water and magnetically stirred rigorously for an hour. The suspension was then dried in an oven and subsequently heated in a Muffle furnace at 700 ^oC with a heat ramp rate of 1.3 ^oC/min for 2.0 h. The furnace was cooled down to RT at slow - cooling rate at of 1 ^oC/min. The end product was the TCN. Without melamine addition, the end product was ACN.

b. Characterization

The crystal structure was characterized by X-ray diffraction (XRD) using a powder X-ray diffractometer (Miniflex, Rigaku) at 40 kV and 15 mA with Cu Kα radiation (λ = 0.154178 nm). Spectroscopy images of a-CN sponge were obtained by SEM (Quanta 450). Transmission electron microscope (TEM) images and selective area diffraction patterns (SAED) were obtained with Tecnai G^2 spirit. N_2 adsorption-desorption measurements were carried out in a BELSORP-max instrument (BELJapan Inc.). An AXIS ultra-spectrometer (Kratos Analytical Ltd., GB) was used to obtain XPS spectra. Optical properties were analyzed from UV-Vis diffuse reflectance spectra (DRS) using UV-Vis spectrophotometer (UV2600, Shimadzu, Japan) in the wavelength of 200 to 800 nm at RT. Photoluminescence (PL) spectra were measured at RT using a fluorescence spectrometer (RF-5301PC, Shimadzu, Japan). A FTIR spectrometer (Nicolet 6700) was used to obtain Fourier transform infra-red spectra. Photoluminescence (PL) spectra were measured at RT using a fluorescence spectrometer (RF-5301PC, Shimadzu, Japan). The femtosecond time resolved data were obtained using a fluorescence upconversion spectrometer in transmission mode (Ultrafast Systems, Halcyone). A Ti:sapphire regenerative amplifier (Spectra-Physics, Spitfire Pro XP 100F) was used as the source of excitation and gate beams, producing pulses with a duration of 100 fs at a 1 kHz

repetition rate. The excitation wavelength of 400 nm was generated by frequency doubling the 800 nm fundamental using a 0.5 mm BBO crystal. The Fourier transform infrared (FTIR) spectrum was recorded on FTIR spectrometer (Nicolet 6700).

c. Photocatalytic H_2 production test

100 mg of photocatalyst was dispersed in 80 mL 10 vol% triethanolamine (TEOA) and Pt was loaded onto the surface of the catalyst by an *in-situ* photodeposition method using H_2PtCl_6 as a precursor. To maintain anaerobic conditions, the openings of the flask were sealed with silicone rubber-septa and the suspension was thoroughly degassed with Ar for 30 min. A Xenon arc lamp (300 W) with a cut-off filter ($\lambda > 420$ nm) was used to achieve visible-light irradiation. Rate of H_2 evolution was evaluated by sampling 0.4 mL of gas intermittently each hour through the septum of an online gas chromatograph (GC) (Clarus 480, PerkinElmer, USA). The GC was equipped with a thermal conductive detector (TCD) with a 5 Å molecular sieve column and Ar as carrier gas. The reactor was evacuated each 4 h of a 12 h recycling period and kept under continuous stirring to prevent sedimentation of the photocatalyst during H_2 production. Before each evacuation, the reaction system was stored in RT for 30 days. Deionized water was used to rinse glassware prior to experiments. Experiments were carried out at ambient temperature and pressure.

The apparent quantum efficiency (AQE) was measured under the same photocatalytic reaction condition. Four low-power 420 nm LEDs which were positioned 1 cm from the reactor in four different directions, were used as light sources to trigger the photocatalytic reaction. The focused intensity for each 420 nm LED was ca. 6.0 mW cm^{-2}. AQE was calculated using Equation 1.

$$AQE(\%) = \frac{2 \times No.\ of\ evolved\ H_2\ molecules}{No.\ of\ incident\ photons} \times 100 \quad (1)$$

d. Photo-electrochemical measurement

The working electrode was prepared by grinding 0.1 g of photocatalyst with 0.03 g of polyethylene glycol (PEG) in 0.5 mL of ethanol to make a slurry. Using a doctor-blade method, the slurry was then coated on the fluorine-doped tin oxide (FTO) glass electrode (3 cm^2) and dried in an oven at 350 ^oC for 30 min under N_2 gas flow. Electrodes coated with slurry had a measured film thickness around 10 to 11 μm. The active area of the electrode was about 1.35

cm^2. The photocurrent and electro-impedance spectroscopy (EIS) measurements were performed in a three-electrode electrochemical system (CHI 650D instruments) where the sample coated FTO was used as a working-electrode whilst Pt and Ag/AgCl were used as a counter- and a reference-electrode, respectively. Transient photocurrent measurement were performed at 0.5 V bias, while a 300 W Xenon arc lamp light was chosen as a light source and 0.2M Na_2S + 0.05 M Na_2SO_3 aqueous solution as electrolyte. The Electro-Impedance Spectroscopy (EIS) measurements were recorded over a 0.005 to 10^5 Hz frequency range with ac amplitude of 10 mV and 0.5 M Na_2SO_4 was used as electrolyte.

E. Fitting Time Resolved Data

We used tri-exponential decay kinetics of Equation S1 to get best fit of the time resolved flourescence data, and used Equation S2 to calculate average tifetime, τ:[1]

$$y = \sum A_i e^{-\frac{t}{\tau_i}} \quad (i = 1,2,3) \tag{S1}$$

$$\tau = \frac{\sum A_i \tau_i^2}{\sum A_i \tau_i} \quad (i = 1,2,3) \tag{S2}$$

where t, τ_i and A_i are constants. The value of these constants is obtained from fitting the decay curves.

F. FDTD Simulation

Lumerical FDTD solutions has been employed to carry out the electromagnetic simulations. Perfectly matched layer (PML) boundary conditions in the x-axis and y-axis was used to set the unit cell of the structure as the simulation region. A plane-wave light source irradiated normally to the device was set to be transverse magnetic (TM) polarized. One monitor was placed between the source plane and device surface in order to detect the device absorption. The current density vectors are collocated at the positions of the electric field vectors.

II. Supplementary Results

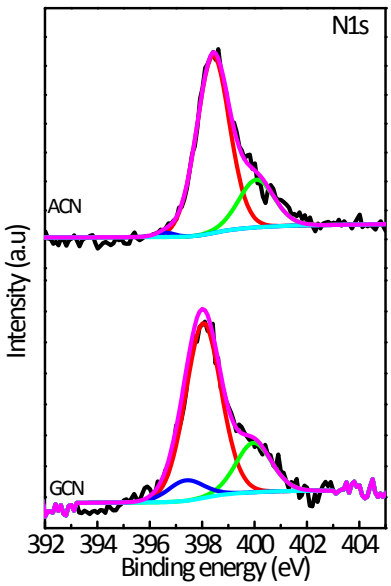

Fig. S1 Deconvoluted N1s spectra.

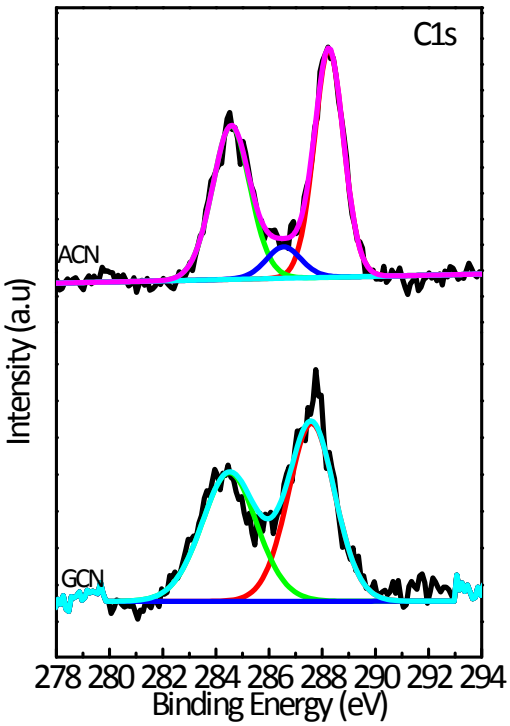

Fig. S2 Deconvoluted C1s spectra.

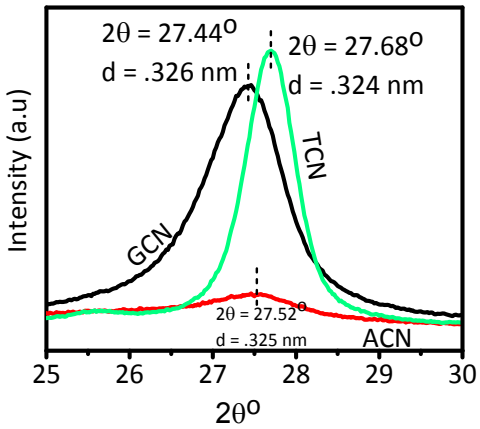

Fig. S3 XRD patterns (extended) of GCN, ACN and TCN.

Previously it was reported that the flat and wide XRD peaks in ACN were the results of breaking of terminal hydrogen bonds in CN matrix and loss of nitrogen through reduction of NH_2 groups.[2, 3] It suggested that 'nitrogen paying back' strategy would regain the crystallinity. We have worked on this hypothesis, and observed that the polycondensation of nitrogen-rich melamine could serve this purpose. The respective XRD and XPS spectra validated our observation. XRD results confirm regaining of crystallinity, and the XPS results provide us the quantitative information about the change in contents of nitrogen and carbon constituents in CN. As is shown in Fig. S3, it is seen that the TCN has the better crystallinity than GCN even as indicated by the sharper XRD peaks and decreased *d*-spacing. This implies that the polycondensation of melamine could repair the crystallinity of amorphous phase. When melamine is undergone polycondensation at high temperature treatment with slow-cooling rate, annealing causes the crystalline regions to grow and slow-cooling rate permits more time for the polymer chains to align and therefore, encourages crystallization. The end benefits of the crystallinity is its paramount impact on reducing the recombination of charge carrier.

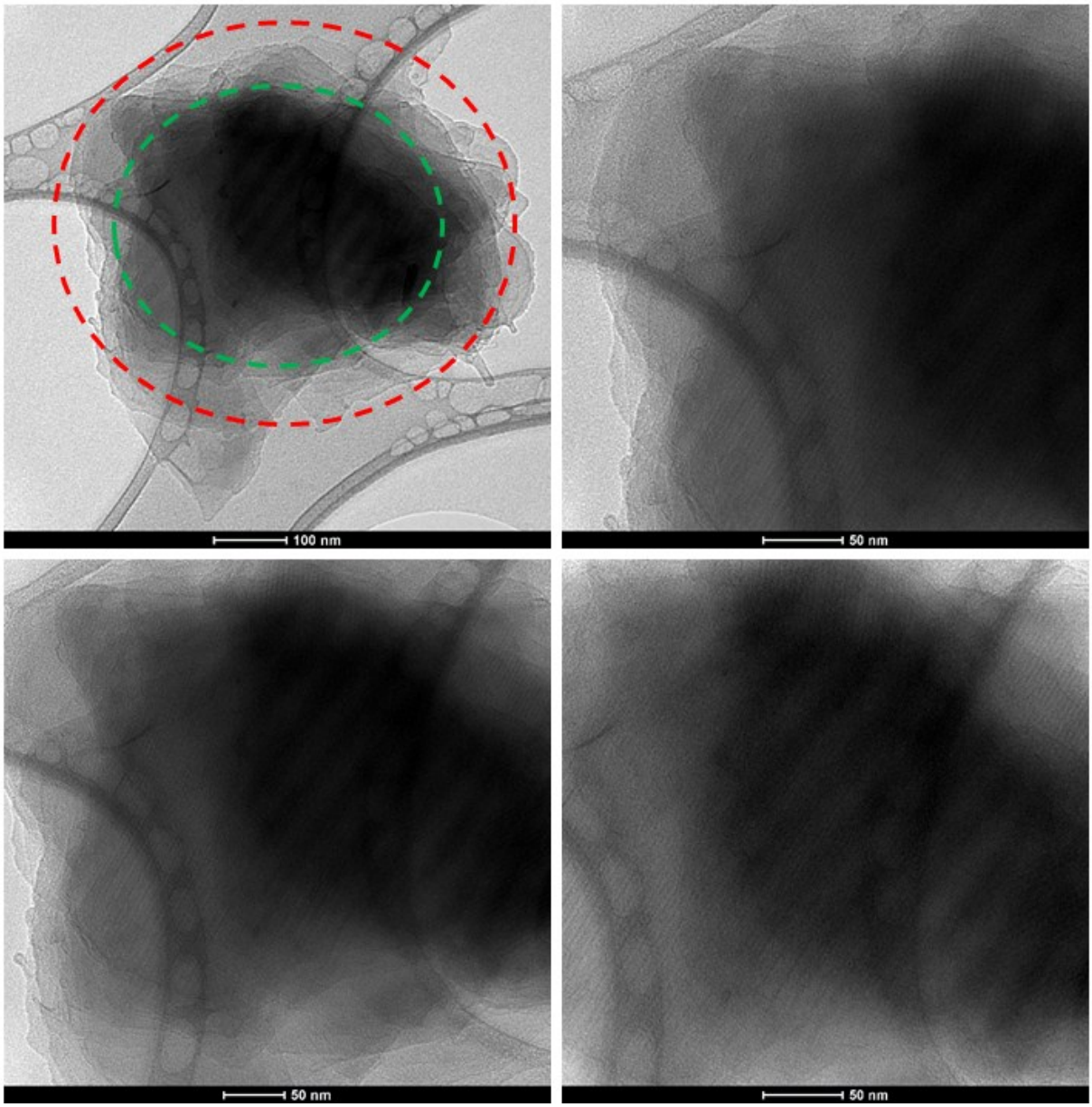

Fig. S4 TEM images of TCN taken at different locations.

The TEM images shows a bulk of TCN which is composed of multilayered nanosheets. There might have polycrystalline and amorphous layers interlinked between the layers. The dark bands, as can be seen in the two images at the bottom (Fig. S4), originated due to accumulation of lattice fringes when congruent on top of one another. This implies that several polycrystalline nanosheets are piled together vertically. This is a good agreement with the structure of polyaniline (C_3N).[4]

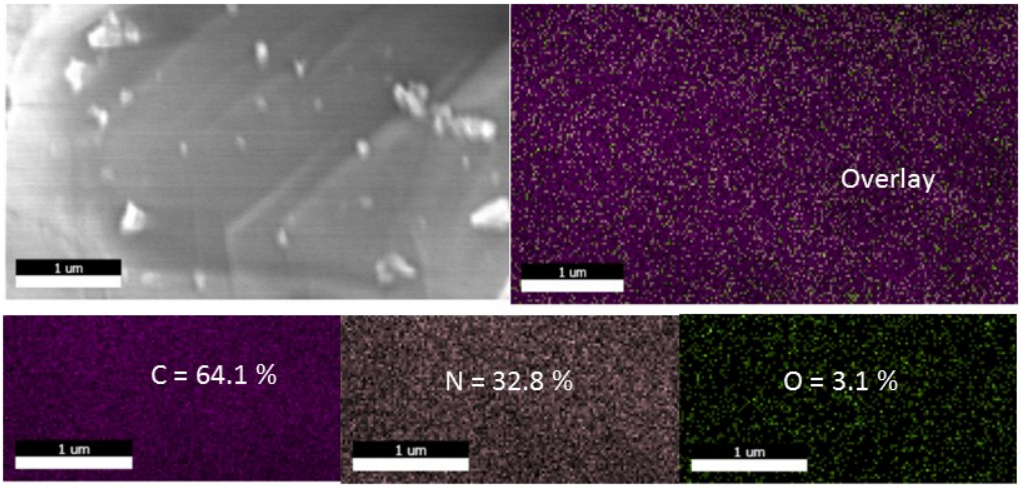

Fig. S5 EDS elemental mapping of TCN.

Table S1 Binding energies (BE) and concentration (%) of core electrons of carbon species calculated from deconvoluted XPS C1s spectra of GCN, ACN and TCN.

	C-N		**C-C**	
	B.E. (eV)	*% conc.*	*B.E. (eV)*	*% conc.*
GCN	288.3	55.5	284.5	45.5
ACN	287.7	67.7	284.6	32.3
TCN	287.5	60.3	284.6	39.7

Table S2 Binding energies (BE) and concentration (%) of core electrons of nitrogen species calculated from deconvoluted XPS N1s spectra of GCN, ACN and TCN.

	Pyrazine/Pyridinic		**Pyrrolic**		**Graphitic**	
	B.E. (eV)	*% conc.*	*B.E. (eV)*	*% conc.*	*B.E. (eV)*	*% conc.*
GCN	398.3	76.4	399.8	20.4	396.5	3.2
ACN	398.2	70.6	400	28.0	396.32	1.4
TCN	397.8	72.4	399.6	27.1	395.85	0.5

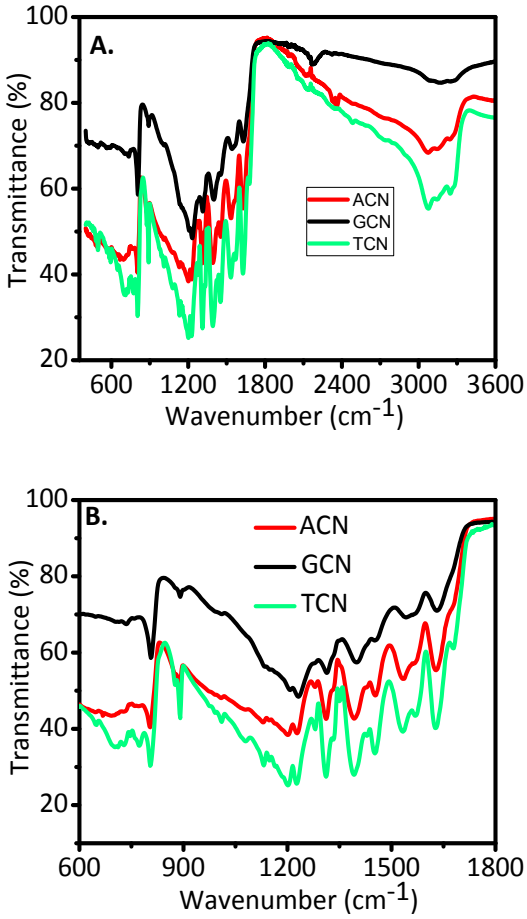

Fig. S6 FTIR Spectra. The vibrational and stretching bands of C-N heterocycles (between 800 to 1700 cm^{-1}) in FTIR spectra for TCN are noticeably pronounced than that of GCN which suggest the repairing of crystallization after polycondensation of melamine. This also supports XRD results. Moreover, the FTIR spectra of GCN and ACN are a good agreement with previously reported results.[3, 5]

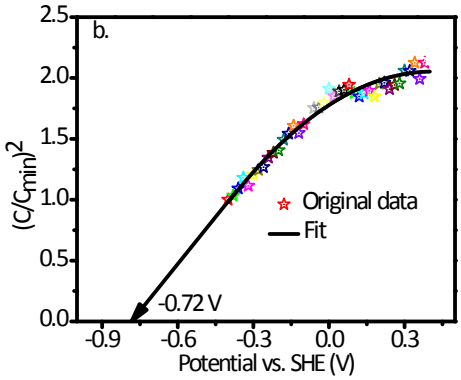

Fig. S7 M-S plot for TCN.

Table S3 Bandgap and band positions of TCN

Bandgap (eV)	**E_{CB} (V vs NHE)**	**E_{VB} (V vs NHE)**
2.75	-0.72	2.03

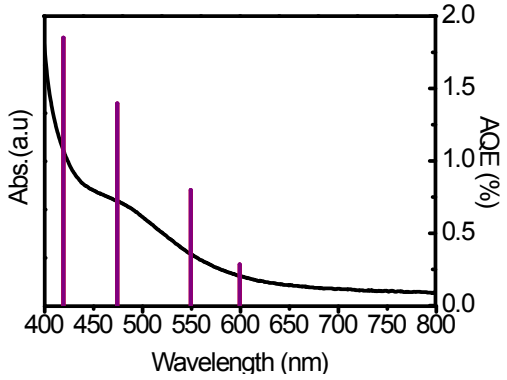

Fig. S8 Wavelength dependent hydrogen production.

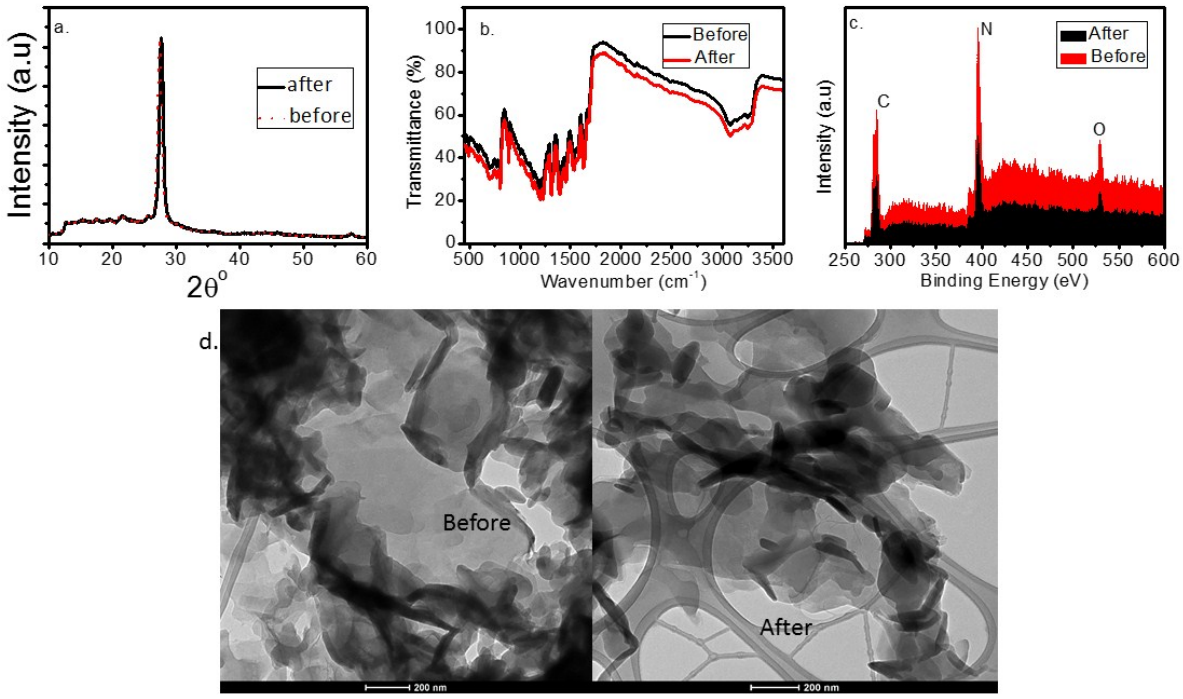

Fig. S9 structural stability of TCN. A) XRD spectra, b) FTIR Spectra, c) XPS spectra, and d) TEM images of fresh and spent samples.

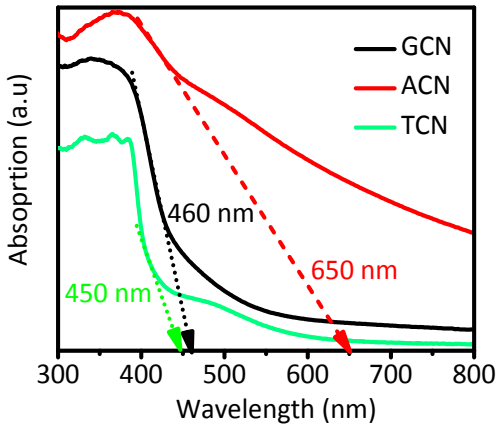

Fig. S10 UV-Vis spectra of GCN, ACN and TCN.

Regardless of restricted or extended photon absorption edges of a photocatalyst, all that it important for enhanced hydrogen production is the availability of photogenerated charge carriers at the photocatalyst/electrolyte interfaces. The rule of thumb is higher the availability of charge carriers, higher is the redox reaction rate. To ensure the handful amount of charge carriers available for redox reactions, along with wider photon absorption window, the photocatalyst must have the ability to save the photogenerated charge carriers (electrons and holes) against odd incident like recombination, and transfer them from the place of generation to the redox reactions sites. Following the absorption of photons of appropriate energy by the photocatalyst, the electrons are excited and lifted to the conduction band (CB) from valence band (VB), leaving behind a hole in the valence band. But the just-excited electrons in conduction band have the natural tendency to fall back to valence band following a series of different recombination processes to maintain the equilibrium (*see* Supplementary Note 1 for a brief overview of different recombination mechanisms in a semiconductor). Recombination is a process of annihilation of the electron-hole pairs (EHP) [6], and hence is considered as very detrimental to the availability of free charge carriers up to the place of reaction sites for reduction and oxidation reactions.[7] We have shown in the main manuscript that despite extended visible light absorption, the low quantum yield of hydrogen in ACN and GCN in compared with TCN was due to high rate of recombination and poor charge transport. (Although TCN has an intrinsic absorption edge of 450 nm). Therefore, unless recombination is inhibited in anyway, wide photon absorption window is less effective.

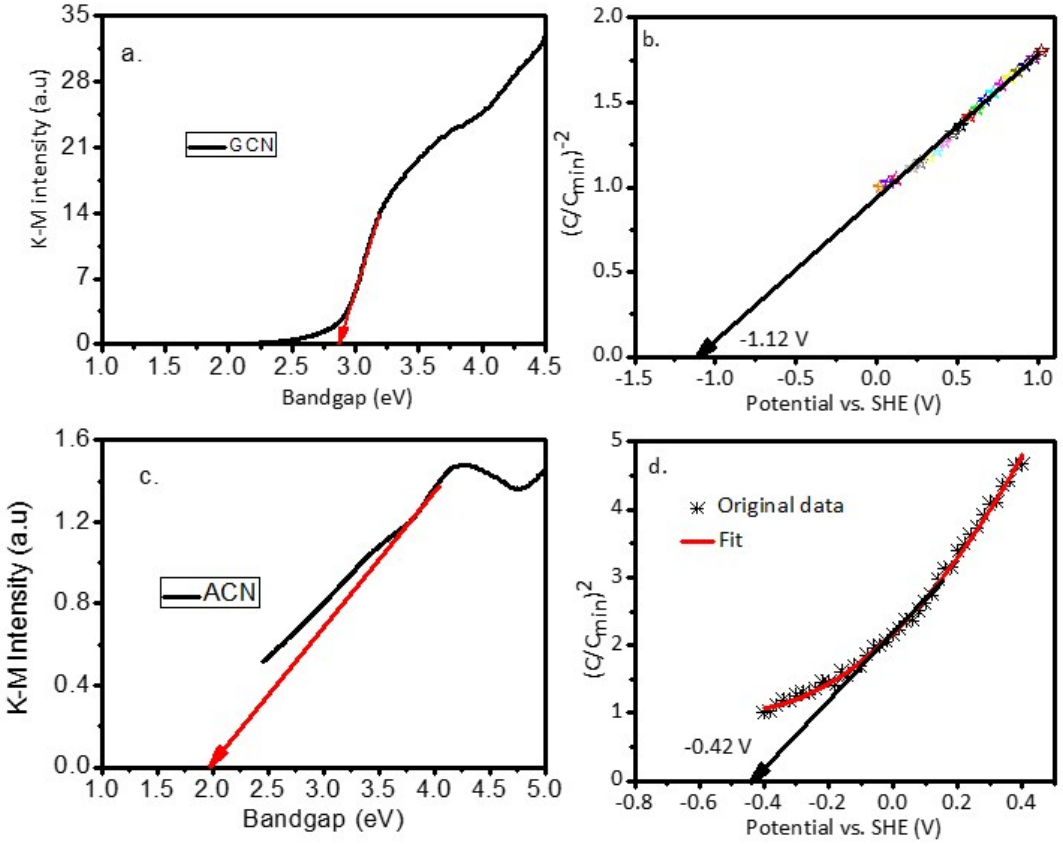

Fig. S11 K-M plot for a) GCN and c) ACN. M-S plot for b) GCN and d) ACN.

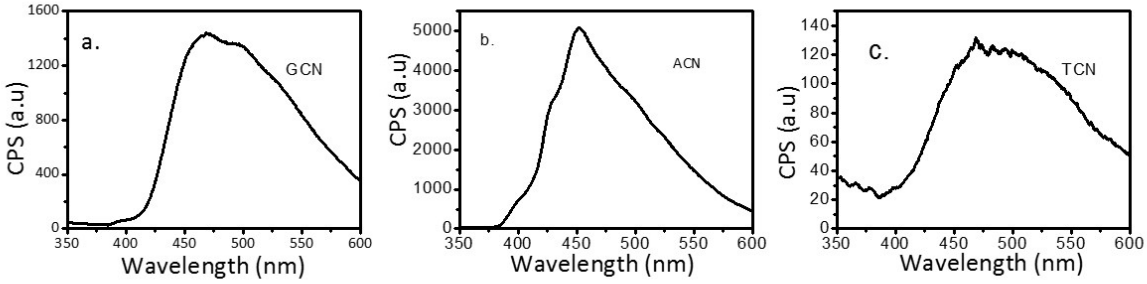

Fig. S12 PL spectra. The excitation wavelength was 325 nm.

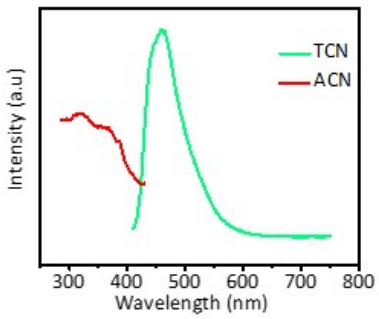

Fig. S13 Emission spectra of TCN and ACN after 400 nm excitation.

Supplementary Note 1: Brief overview of Recombination mechanisms in semiconductor, and suppression of recombination in TCN

Recombination is a process when electrons meet holes in a material. When electron meets hole, they both are annihilated. That's why recombination is considered very detrimental for semiconductor materials where both electron and hole have the contribution in current conduction.

The recombination mechanisms in a semiconductor are mainly two types, intrinsic and extrinsic. Intrinsic recombination is of two kinds, radiative and Auger recombination. Extrinsic recombination is of also two kinds, Shockley-Read-Hall (SRH) and surface recombination. A chart of the recombination mechanisms are shown in Fig.S14. Intrinsic recombination is the inherent recombination which no semiconductor can avoid. It indicates that a semiconductor with no recombination of charge carrier never can exist. Extrinsic recombination is governed by crystallinity, defects, vacancies and dangling bonds etc. developed within a semiconductor. It is therefore possible to overcome the extrinsic recombination fully or partially.

In a semiconductor, all the stated recombination mechanisms or only selected recombination can active at a time. It depends on the materials properties and types of semiconductor. For example, radiative recombination is the dominative recombination in direct-semiconductors whereas it is less-prevailed in indirect-semiconductors. Main characteristics of each type of recombination is discussed below.[8]

Radiative recombination is a band-band recombination which involve the direct annihilation of electron-hole pair and emission (release of excess energy) of photon with an energy more or less equal to that of bandgap energy. It is an inverse process of optical generation of charge carriers, and therefore, depends jointly on the concentrations of free electrons and holes.

Auger recombination is a three-particle recombination process. In this recombination process, the excess energy that release from the recombination of electro-hole pair is transferred to third free carrier, the transition thus being non-radiative. This third carrier then release its excess energy as phonons to the crystal as thermal energy. Depending on the third carrier being either an electron or hole, Auger recombination can be an electron-electron-hole or electron-hole-hole process.

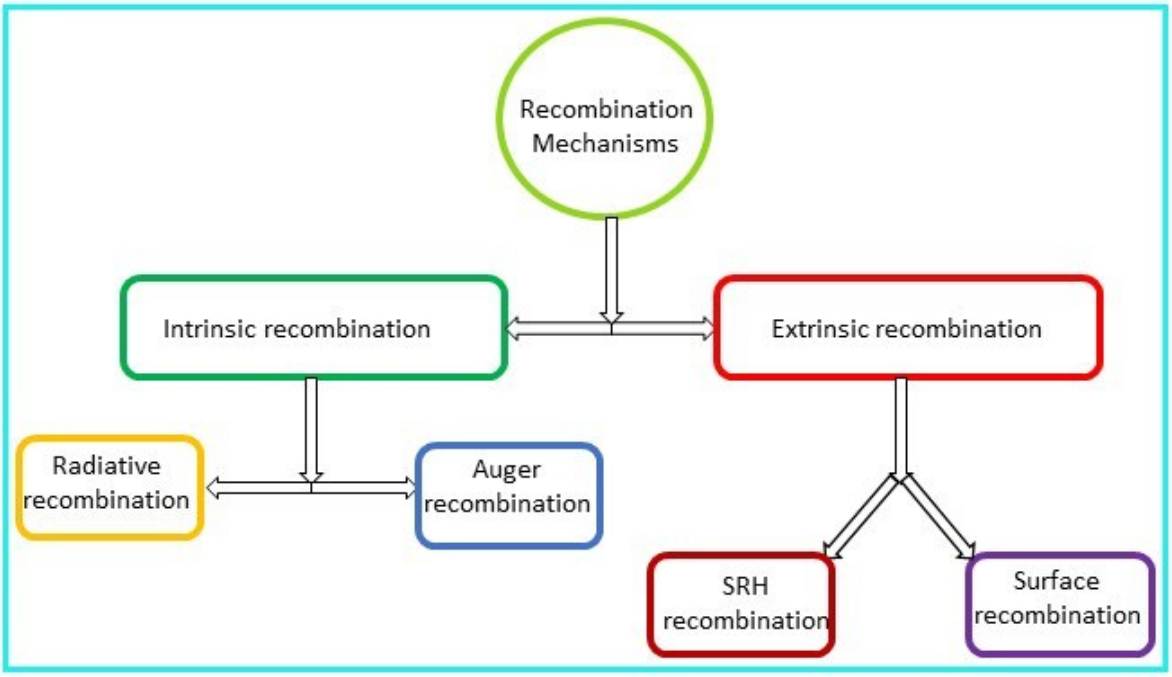

Fig.S14 Chart of recombination mechanisms in a semiconductor.

Both *SRH and surface recombination* is defect assisted recombination. When the recombination is due to the defects in bulk (e. g. impurities or crystal imperfections) is named after the inventors Shockley, Read and Hall (SRH). When the recombination is due to the surfaces or interfaces states that present an abrupt discontinuity in crystal structure is termed as surface recombination. These defects produces discrete energy levels within the bandgap and act as recombination/trap centres.

It is now clear that recombination is depend on material properties. By modifying crystal structure and electronic properties of the certain material, it is possible to reduce the recombination rate. [6, 9] Usually, materials with low density of crystal defects, grain and grain boundaries are less prone to recombination mechanisms. Hence, increasing the crystallinity of the materials is one of the ways to avoid recombination to some extent.[10] In the XRD patterns (Fig. 1A), the characteristic peaks at (100) plane and (002) plane of TCN are noticeably sharper than that of GCN and ACN. It suggests that TCN is more crystalline than both GCN and ACN. Moreover, as shown in Fig 1B, there are some additional peaks can be observed between $10^{o}<2\Theta<24^{o}$, indicating the increased crystallinity of the TCN hybrid.[11] With increasing crystallinity, the d-space becomes decreased which reduces the diffusion length of the charge carrier and is equivocally beneficial to reduce the recombination as well.[12, 13] As shown in Fig. S3, the d-spacing for GCN, ACN and TCN is 3.26 nm, 3.25 nm and

3.24 Å, respectively. This implies that TCN earns a background to have suppressed recombination of electron-hole pairs.

Readily we have checked the extent of reduction of charge carrier recombination by measuring respective photoluminescence (PL) spectra of GCN, ACN and TCN. Compare to GCN and ACN, PL intensity of TCN is greatly reduced, meaning that radiative recombination of EHP is drastically suppressed in TCN.[14] It is because, in TCN an electric potential-barrier formed within the junction between two complementary phases which facilitates the electrons accumulation in one side of the junction and the holes in the other side, thus prevent electron-hole meeting. This therefore efficiently reduce the charge carrier recombination probability.[15, 16]

Supplementary Note 2: Determinant of improved H_2 production rate

Table S4 Summery of physicochemical attributes of TCN, GCN and ACN

Photocatalyst	Absorption Edge (nm)	S_{BET} (m^2/gm)	Electron lifetime (ns)	Pt loading (wt. %)	H_2 production (µmol h^{-1})	AQE (%)
TCN	450	39.4	16.18	0	31	1.86
GCN	460	12.5	1.34	1	27	1.62
ACN	650	51	0.16	1	18	1.1

Note: Red-filled cell indicates the highest value while yellow indicates the lowest.

We have summarized the optical, electronic, surface area and photocatalytic conditions of TCN, GCN and CAN in Table S4 for identification of the crucial determinant in enhanced hydrogen production. With a close look to tabulated data, it is safe to conclude that ability of suppress recombination and efficient charge transport of a given photocatalyst is the ultimate game changer in photocatalytic reactions. For example, ACN showed highest absorption edge and BET surface area, but had lowest hydrogen evolution rate.

Supplementary Note 3: Bulk is convenient in photocatalysis

Using bulk phase photocatalyst in solar hydrogen production is always convenient. However, photocatalytic performance of most of the photocatalysts in bulk form was not satisfactory. It led researchers to explore 1D, 2D or the various combination of 1D/2D architectures out of bulk materials. One of the major disadvantages of the 1D and 2D counterpart of bulk material is their inevitably complex synthesis processes. In many cases, synthesis of the proposed 1D

or 2D structure is also not reproducible in exact shape and size. In addition, it is absolutely difficult to maintain uniform dispersity of nanomaterial during catalytic action. Rather, they aggregated and behaved like a bulk-phase material. Unfortunately, reproducibility and aggregation effects is somewhat overlooked in photocatalytic research community. The dispute of nanomaterials would not be an issue if reasonably acceptable performance could attain through employing bulk-photocatalysts.

TCN is a bulk materials which are clearly evident by SEM and TEM images (Fig. S4 and S15). The photocatalytical hydrogen production manifests that it is possible to attain high performance in bulk-phase without cocatalyst even.

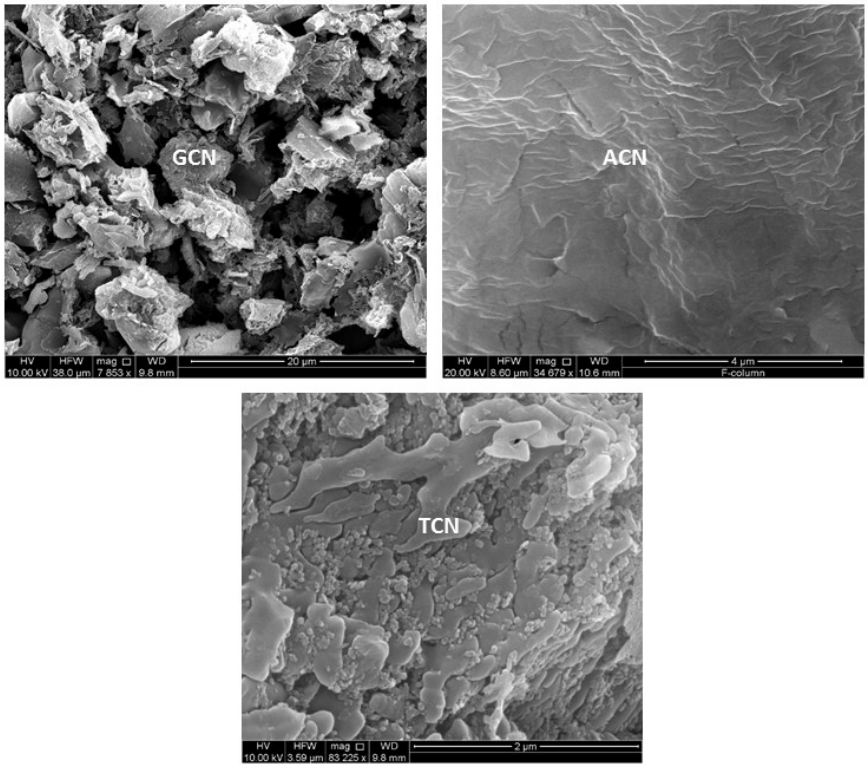

Fig. S15 SEM images of GCN, ACN and TCN.

Appendix S1: Atomic co-ordination of TCN

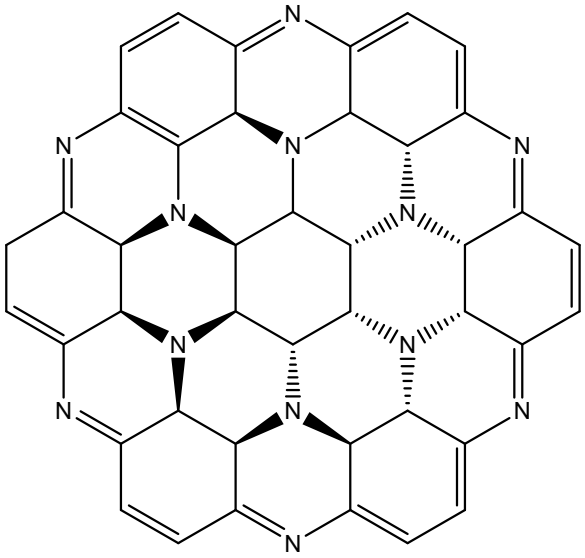

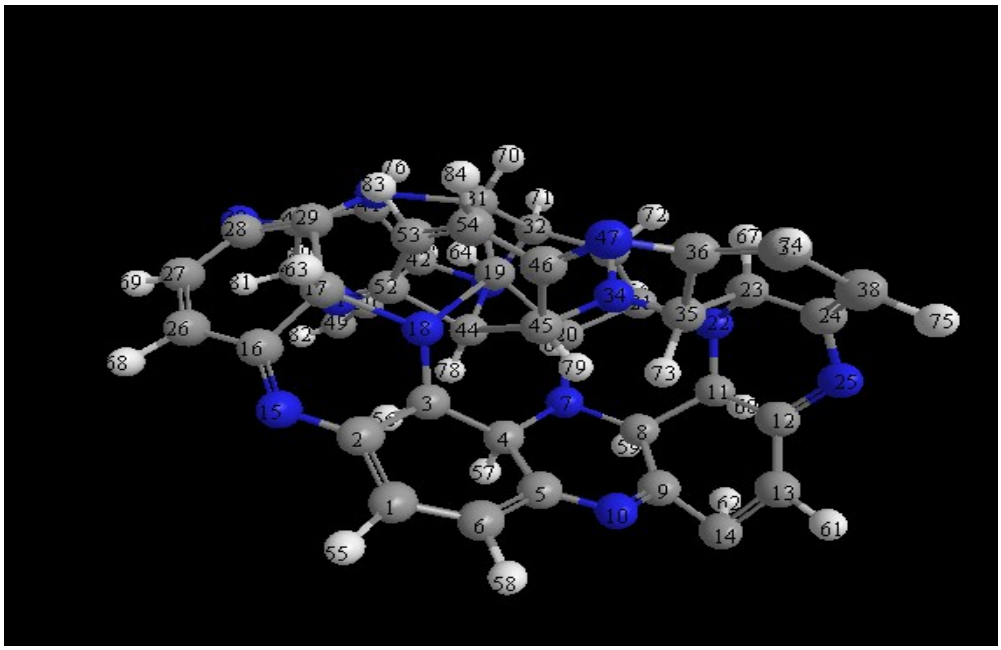

Atom	Bond Atom	Bond Length (Å)	Angle Atom	Angle (°)
C(1)				
C(2)	C(1)	1.337		
C(3)	C(2)	1.497	C(1)	121.3997
C(6)	C(1)	2.4744	C(2)	57.2444
N(15)	C(2)	1.26	C(1)	123.4988
C(5)	C(6)	1.337	C(1)	98.9778
C(16)	N(15)	1.26	C(2)	115
H(55)	C(1)	1.1	C(2)	151.378
C(4)	C(5)	1.497	C(6)	121.4001
C(17)	C(16)	1.4853	N(15)	116.3025

N(7)	C(4)	1.438	C(3)	109.4697
N(18)	C(3)	0.5405	C(2)	133.9927
C(19)	N(18)	1.438	C(3)	107.7
C(29)	C(17)	1.497	C(16)	109.47
C(28)	C(29)	1.337	C(17)	121.4002
N(30)	C(29)	1.266	C(17)	125.2984
C(8)	N(7)	1.438	C(4)	107.6998
C(20)	N(7)	1.438	C(4)	107.7006
C(21)	C(20)	1.523	N(7)	109.4696
C(31)	C(19)	1.523	N(18)	109.4702
C(32)	C(31)	1.523	C(19)	109.4697
C(41)	N(30)	1.47	C(29)	107.9999
C(9)	C(8)	1.4757	N(7)	115.4861
C(11)	C(8)	1.523	N(7)	109.47
C(12)	C(11)	1.497	C(8)	109.4699
N(22)	C(11)	1.438	C(8)	109.4701
C(23)	N(22)	1.438	C(11)	107.7003
C(33)	C(21)	1.523	C(20)	109.4699
N(34)	C(33)	1.438	C(21)	109.47
N(43)	C(32)	1.438	C(31)	109.4702
C(24)	C(23)	1.4252	N(22)	119.0646
C(35)	C(23)	1.523	N(22)	109.47
C(36)	C(35)	1.497	C(23)	109.4698
C(45)	N(34)	1.438	C(33)	107.7
C(40)	C(41)	1.5379	N(30)	108.8605
C(42)	C(41)	1.523	N(30)	110.7403
C(44)	N(43)	1.438	C(32)	107.7002
C(46)	C(45)	1.497	N(34)	110.7402
C(50)	C(42)	1.497	C(41)	109.4706
C(52)	C(44)	1.497	N(43)	110.7404
N(10)	C(5)	1.26	C(4)	115.0986
C(14)	C(9)	1.337	C(8)	121.4002
C(26)	C(16)	1.337	N(15)	123.4985
C(27)	C(26)	2.3862	C(16)	72.5209
N(39)	C(28)	1.26	C(27)	119.9984
C(48)	C(40)	1.497	N(39)	161.9973
C(13)	C(14)	3.0579	C(9)	56.2259
N(25)	C(12)	1.26	C(11)	115.0991
C(38)	C(24)	1.337	C(23)	121.3981
C(37)	C(38)	2.6875	C(24)	87.1855
N(47)	C(36)	1.26	C(35)	115.0994
C(54)	C(46)	1.337	C(45)	121.4001
C(49)	C(48)	0.6369	C(40)	131.3744
N(51)	C(50)	1.26	C(42)	115.0992
C(53)	C(52)	1.337	C(44)	121.3981
H(61)	C(13)	1.1	C(12)	130.2672

H(62)	C(14)	1.1	C(9)	151.8867
H(68)	C(26)	1.1	C(16)	143.7392
H(69)	C(27)	1.1	C(26)	131.4906
H(74)	C(37)	1.1	C(36)	139.3299
H(75)	C(38)	1.1	C(24)	136.4072
H(82)	C(49)	1.1	C(48)	121.9434
H(83)	C(53)	1.1	C(52)	150.496
H(84)	C(54)	1.1	C(46)	129.4985
H(58)	C(6)	1.1	C(1)	130.5115
H(56)	C(3)	1.113	C(2)	86.9671
H(57)	C(4)	1.113	C(3)	109.9085
H(59)	C(8)	1.113	N(7)	108.6177
H(60)	C(11)	1.113	C(8)	109.9087
H(63)	C(17)	1.113	C(16)	109.0521
H(64)	C(19)	1.113	N(18)	123.1989
H(65)	C(20)	1.113	N(7)	145.3885
H(66)	C(21)	1.113	C(20)	132.1244
H(67)	C(23)	1.113	N(22)	108.618
H(70)	C(31)	1.113	C(19)	151.0044
H(71)	C(32)	1.113	C(31)	124.7722
H(72)	C(33)	1.113	C(21)	116.7516
H(73)	C(35)	1.113	C(23)	69.6499
H(76)	C(41)	1.113	N(30)	108.0457
H(77)	C(42)	1.113	C(41)	123.0034
H(78)	C(44)	1.113	N(43)	109.0692
H(79)	C(45)	1.113	N(34)	144.2741
H(80)	C(48)	1.113	C(40)	103.7355
H(81)	C(48)	1.113	C(40)	96.836

Appendix S2: Atomic co-ordination of GCN

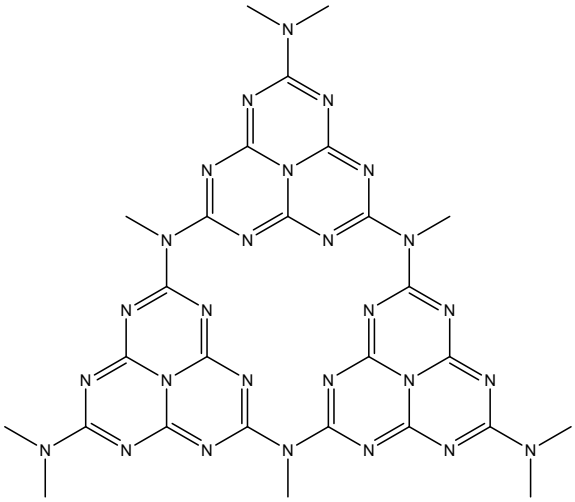

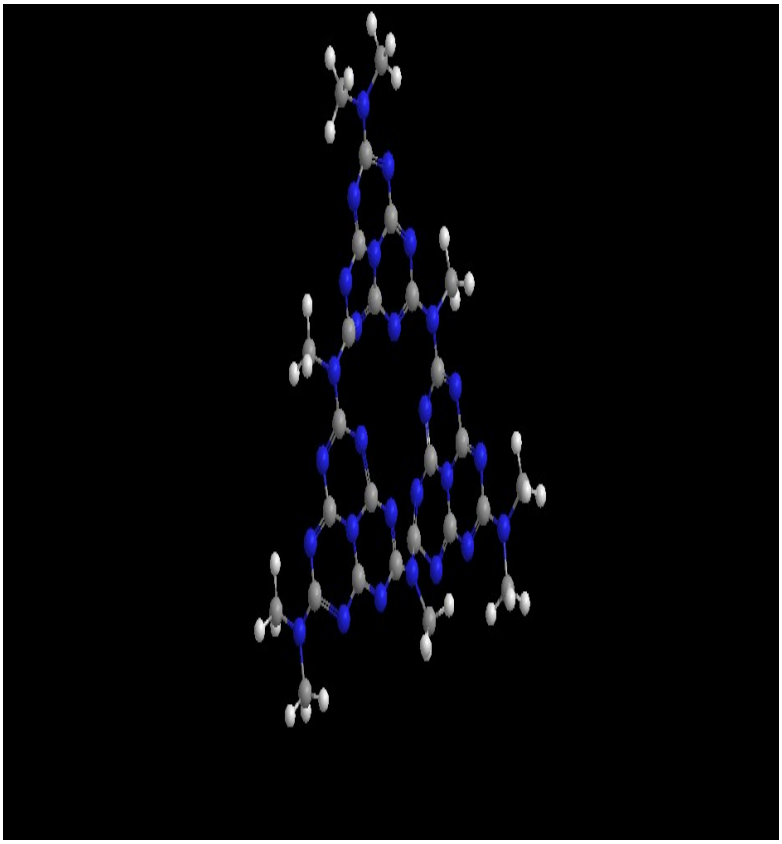

Atom	Bond Atom	Bond Length (Å)	Angle Atom	Angle (°)
N(1)				
C(2)	N(1)	1.26		
N(3)	C(2)	1.266	N(1)	126.0001
N(7)	C(2)	1.26	N(1)	107.9993
C(6)	N(1)	1.26	C(2)	115.0001
C(4)	N(3)	1.266	C(2)	123.9999
C(10)	N(3)	1.266	C(2)	123.9989
N(5)	C(6)	1.9359	N(1)	120.7567

N(45)	C(6)	1.266	N(1)	119.6218
N(13)	C(4)	1.5744	N(3)	114.9902
C(12)	N(13)	1.26	C(4)	113.2088
C(8)	N(7)	1.26	C(2)	114.9999
N(9)	C(10)	1.26	N(3)	126.0003
N(11)	C(10)	1.26	N(3)	125.9984
N(20)	C(8)	1.266	N(7)	118.5831
N(34)	C(12)	1.266	N(11)	119.9986
C(19)	N(20)	1.266	C(8)	124.0001
C(51)	N(20)	1.47	C(8)	118.0001
N(14)	C(19)	1.26	N(20)	119.9997
N(18)	C(19)	1.26	N(14)	119.9991
C(15)	N(14)	1.26	C(19)	114.9998
C(17)	N(18)	1.5786	C(19)	118.5024
N(16)	C(17)	1.266	N(18)	98.4877
N(27)	C(17)	1.26	N(16)	125.9976
N(21)	C(15)	1.26	N(14)	107.9993
C(22)	N(21)	1.26	C(15)	115
C(24)	N(16)	1.266	C(15)	123.9987
N(23)	C(24)	1.26	N(16)	125.9985
N(46)	C(22)	1.266	N(21)	121.2157
N(25)	C(24)	1.26	N(16)	126
C(26)	N(25)	1.6135	C(24)	104.9324
N(42)	C(26)	1.266	N(25)	144.1686
C(33)	N(34)	1.266	C(12)	124.0001
C(43)	N(34)	1.47	C(12)	117.9997
N(28)	C(33)	1.26	N(34)	119.9999
N(32)	C(33)	1.26	N(28)	119.9988
C(31)	N(32)	1.3936	C(33)	126.388
C(29)	N(28)	1.26	C(33)	114.9999
N(30)	C(29)	1.266	N(28)	126.0003
N(35)	C(29)	1.26	N(28)	107.9993
C(38)	N(30)	1.266	C(29)	123.9987
N(41)	C(31)	1.26	N(30)	126.1836
C(40)	N(41)	1.26	C(31)	114.9996
C(36)	N(42)	1.266	C(26)	124.0004
N(37)	C(38)	1.26	N(30)	126.0002
N(39)	C(38)	1.26	N(30)	125.9985
N(44)	C(40)	1.266	N(39)	118.1908
C(52)	N(42)	1.47	C(26)	117.9998
C(47)	N(45)	1.47	C(6)	119.9999
C(48)	N(45)	1.47	C(6)	120.0002
C(49)	N(46)	1.47	C(22)	120.0006
C(50)	N(46)	1.47	C(22)	119.9993
C(53)	N(44)	1.47	C(40)	119.9993
C(54)	N(44)	1.47	C(40)	120.0005

H(55)	C(43)	1.113	N(34)	109.5001
H(56)	C(43)	1.113	N(34)	109.4421
H(57)	C(43)	1.113	N(34)	109.4616
H(58)	C(47)	1.113	N(45)	109.5004
H(59)	C(47)	1.113	N(45)	109.4421
H(60)	C(47)	1.113	N(45)	109.4618
H(61)	C(48)	1.113	N(45)	109.5003
H(62)	C(48)	1.113	N(45)	109.442
H(63)	C(48)	1.113	N(45)	109.4622
H(64)	C(49)	1.113	N(46)	109.4998
H(65)	C(49)	1.113	N(46)	109.4423
H(66)	C(49)	1.113	N(46)	109.4625
H(67)	C(50)	1.113	N(46)	109.5001
H(68)	C(50)	1.113	N(46)	109.4416
H(69)	C(50)	1.113	N(46)	109.4617
H(70)	C(51)	1.113	N(20)	109.4999
H(71)	C(51)	1.113	N(20)	109.4416
H(72)	C(51)	1.113	N(20)	109.462
H(73)	C(52)	1.113	N(42)	109.4996
H(74)	C(52)	1.113	N(42)	109.4415
H(75)	C(52)	1.113	N(42)	109.4614
H(76)	C(53)	1.113	N(44)	109.5002
H(77)	C(53)	1.113	N(44)	109.441
H(78)	C(53)	1.113	N(44)	109.4616
H(79)	C(54)	1.113	N(44)	109.5
H(80)	C(54)	1.113	N(44)	109.4419
H(81)	C(54)	1.113	N(44)	109.4622

References

1. K. Wu, Y. Du, H. Tang, Z. Chen and T. Lian, *J. Am. Chem. Soc.*, 2015, **137**, 10224-10230.
2. Y. Kang, Y. Yang, L. C. Yin, X. Kang, L. Wang, G. Liu and H. M. Cheng, *Adv. Mater.*, 2016, **28**, 6471.
3. Y. Kang, Y. Yang, L.-C. Yin, X. Kang, G. Liu and H.-M. Cheng, *Adv. Mater.*, 2015, **27**, 4572-4577.
4. J. Mahmood, E. K. Lee, M. Jung, D. Shin, H.-J. Choi, J.-M. Seo, S.-M. Jung, D. Kim, F. Li, M. S. Lah, N. Park, H.-J. Shin, J. H. Oh and J.-B. Baek, *Proc. Nat. Acad. Sci., U.S.A*, 2016, **113**, 7414-7419.
5. M. Zhang and X. Wang, *Energy Environ. Sci.*, 2014, **7**, 1902-1906.
6. M. Z. Rahman, *Renewable Sustainable Energy Rev.*, 2014, 30, 734-742.
7. J. Albero, E. M. Barea, J. Xu, I. Mora-Seró, H. Garcia and M. Shalom, *Adv. Mater. Interfaces* 2016, **3**, 1600265.
8. S. Rein, *Lifetime Spectroscopy - A Method for Defetc Characterization in Silicon for Photovoltaic Applications*, Springer-Verlag, 2005.
9. M. Z. Rahman and S. I. Khan, *Mater. Renew. Sust. Energy*, 2012, 1, 1-11.
10. K. Schwinghammer, M. B. Mesch, V. Duppel, C. Ziegler, J. Senker and B. V. Lotsch, *J. Am. Chem. Soc.*, 2014, **136**, 1730-1733.
11. D. Foy, G. Demazeau, P. Florian, D. Massiot, C. Labrugère and G. Goglio, *J. Solid State Chem.*, 2009, **182**, 165-171.
12. S. C. Warren, K. Voïtchovsky, H. Dotan, C. M. Leroy, M. Cornuz, F. Stellacci, C. Hébert, A. Rothschild and M. Grätzel, *Nat. Mater.*, 2013, **12**, 842-849.
13. Y. Cui, G. Zhang, Z. Lin and X. Wang, *Appl. Catal B: Environ.*, 2016, **181**, 413-419.
14. M. Z. Rahman, J. Ran, Y. Tang, M. Jaroniec and S. Z. Qiao, *J. Mater. Chem. A*, 2016, **4**, 2445-2452.
15. A. V. Akimov, A. J. Neukirch and O. V. Prezhdo, *Chem. Rev.*, 2013, **113**, 4496-4565.
16. J. Zhang, M. Zhang, R.-Q. Sun and X. Wang, *Angew. Chem. Int. Ed.*, 2012, **51**, 10145-10149.